

# Molecular Structure, Spin Density Distribution, and Hyperfine Coupling Constants of the $\eta^1\{\text{CuNO}\}^{11}$ Adduct in the ZSM-5 Zeolite: DFT Calculations and Comparison with EPR Data

P. Pietrzyk, W. Piskorz, and Z. Sojka\*

Faculty of Chemistry, Jagiellonian University, Ingardena 3, 30-060 Cracow, Poland

E. Broclawik

Institute of Catalysis and Surface Chemistry, Polish Academy of Sciences, Niezapominajek 8, 30-239 Cracow, Poland

Received: January 22, 2003; In Final Form: April 17, 2003

DFT calculations of the molecular structure of the intrazeolite  $\eta^1\{\text{CuNO}\}^{11}$  adduct and the  $^{14}\text{N}$  and  $^{17}\text{O}$  hyperfine and  $^{63}\text{Cu}$  superhyperfine coupling constants were performed and compared with previous EPR results. The calculations confirmed the choice of signs adopted in the previous analysis of the experimental data and the character of the SOMO. The influence of the basis set and the exchange-correlation functional on the HFCC and the spin-density distribution was investigated and briefly discussed. The global repartition of the spin density over Cu ( $\rho = 0.11$ ), N ( $\rho = 0.58$ ), and O ( $\rho = 0.34$ ) atoms determined from the Mulliken population analysis compared well with the experiment. The  $^{14}\text{N}$  hyperfine tensor was successfully reproduced with the LanL2DZ basis and BPW91 functional, whereas in the case of the  $^{63}\text{Cu}$  superhyperfine dipolar tensor  $T$  the agreement, except for that of the  $T_{zz}$  component, was less satisfactory because of an overestimated polarization of the  $3d_{yz}$  orbital, regardless of the computation level. For the calculation of  $a_{\text{iso}}$  (Cu), because LanL2DZ treats inner electrons with the effective core potential, a 6-311G(df) basis set appeared to be the most appropriate, leading to excellent agreement between the experimental and calculated values.

## 1. Introduction

Recent interest in copper nitrosyl complexes formed in ZSM-5 zeolites has been undoubtedly motivated by the discovery of the CuZSM-5 catalyst for  $\text{NO}_x$  decomposition.<sup>1</sup> Particular attention has been devoted to copper mononitrosyl  $\eta^1\{\text{CuNO}\}^{11}$  species as one of the possible key intermediates of that reaction.<sup>2,3</sup> Among the different spectroscopic methods applied to the investigation of the intrazeolite  $\eta^1\{\text{CuNO}\}^{11}$  adduct, EPR spectroscopy has been used extensively because this adduct is paramagnetic and gives rise to well-resolved spectra with  $^{63}\text{Cu}$  and  $^{14}\text{N}$  hyperfine splittings.<sup>2,4</sup> An interpretation of the hyperfine parameters in terms of the geometry and electronic structure of the  $\eta^1\{\text{CuNO}\}^{11}$  adduct provides substantial chemical information that is useful in understanding the reactivity of this intermediate. Such an analysis involving the decomposition of the experimental hyperfine tensors into isotropic and anisotropic components essentially depends on a correct assumption of their signs. Unfortunately, this information is not available from the EPR spectra, and the signs of the hyperfine components have to be deduced using judicious theoretical arguments. Furthermore, because of the low  $C_s$  symmetry of the adduct, the effects related to the noncoincidence of the principal axes of the  $g$  and hyperfine  $A$  tensors ought to be recognized correctly, which is not a trivial task in the case of the powder spectra.<sup>5</sup> Therefore, taking the available EPR parameters as computational targets, these data may be further complemented and detailed by suitable quantum chemical calculations. How-

ever, a successful reproduction of the  $g$  tensor and hyperfine coupling constants (HFCCs) can be taken as a reliable confirmation of the adequacy of the adopted cluster model and the calculation scheme as well. Even in the cases where the agreement with experiment is less satisfactory, such calculations can at least help to predict the signs of the hyperfine components and provide some hints concerning the orientation of the principal axes of the corresponding tensors with respect to the molecular axes of the paramagnetic species.

Theoretical studies of HFCCs have focused mostly on organic compounds<sup>6–9</sup> or systems composed of light elements<sup>10–12</sup> because an accurate inclusion of the electron-correlation effects, which is indispensable to the obtaining of acceptable results, is computationally quite demanding. Of the many *ab initio* approaches, the MRCI, QCI, and coupled cluster (CC) techniques in conjunction with large basis sets have proven to reproduce HFCCs with sufficient accuracy.<sup>8</sup> Being quite involved, they are, however, restricted to relatively small systems. An alternative approach of calculating HFCCs is offered by the density functional theory (DFT), which approximately includes the electron correlation and exchange so that transition metals can be taken into account at moderate computational cost.<sup>13–15</sup> This method, combined with the finite cluster model, has recently been used more and more to calculate HFCCs and  $g$  tensors for a number of molecular and nonmolecular systems such as  $\text{VO}(\text{H}_2\text{O})_5$ ,<sup>16</sup> molybdenum oxyhalide ions,<sup>17</sup> Co and Ni complexes,<sup>18</sup>  $d^1$  metal porphyrins,<sup>19</sup>  $\text{Cu}^{2+}$  in A and Y zeolites,<sup>20</sup> and  $\text{VO}^{2+}$  in ZSM-5.<sup>21</sup>

We report herein the results of “pure” and hybrid density functional calculations of the molecular structure and HFCCs

\* To whom correspondence should be addressed. E-mail: sojka@chemia.uj.edu.pl.

of the  $\eta^1\{\text{CuNO}\}^{11}$  adduct formed upon the adsorption of NO on the Cu<sup>I</sup>ZSM-5 zeolite at low pressure. The principal goals of the paper were to corroborate the previous analysis of the experimental EPR spectrum, to detail the geometry of this adduct, to reproduce the experimental hyperfine  $^{63,65}\text{Cu}$  and  $^{14}\text{N}$  tensors, and to predict the  $^{17}\text{O}$  tensor. Furthermore, the influence of the basis sets and different exchange-correlation functionals ( $\nu_{\text{xc}}[\rho]$ ) on the calculated HFCC parameters was also examined. The intrazeolite  $\eta^1\{\text{CuNO}\}^{11}$  adduct studied herein is one of the largest copper-containing nonmolecular systems for which the HFCC calculations were performed. It thus proffers a severe test for both the efficiency and the accuracy of the currently available calculation schemes, strengthened by the fact that copper is one of the most demanding elements for such calculations among the first-row transition metals.<sup>13</sup> It is worth noting here that earlier HF calculations of HFCCs for a smaller  $\{\text{Cu}(\text{NH}_3)\text{NO}\}$  complex using a double- $\zeta$ -quality basis set and configuration interaction with all single and double excitations (CISD) were able to reproduce the nitrogen isotropic coupling constant, but they completely failed in the case of copper  $a_{\text{iso}}$ . This was mainly caused by an inadequate description of the spin polarization of the core  $s$  orbitals, which can contribute significantly to the observed HFCC without playing an appreciable role in the SOMO (singly occupied molecular orbital) composition.<sup>22</sup>

## 2. Theoretical and Computational Approach

The EPR spectrum of the  $\eta^1\{\text{CuNO}\}^{11}$  adduct can be rationalized in terms of the following Hamiltonian:

$$\hat{H} = \beta_e \mathbf{B}^T \mathbf{g} \hat{\mathbf{S}} + \sum_{n=\text{Cu}, \text{N}} \hat{\mathbf{S}}^T \mathbf{A}^n \hat{\mathbf{I}} \quad (1)$$

In this formalism, the  $\mathbf{g}$  tensor parametrizes the interaction between the effective magnetic moment of the paramagnet with the external magnetic field  $\mathbf{B}$ . The hyperfine coupling tensor  $\mathbf{A}^n$  is usually factorized into isotropic ( $a_{\text{iso}}$ ) and anisotropic ( $\mathbf{T}$ ) components:

$$\mathbf{A}^n = a_{\text{iso}}^n \mathbf{E} + \mathbf{T}^n \quad (2)$$

The isotropic constant (Fermi contact term) is directly proportional to the spin density  $\rho^{\alpha-\beta}(r_n) \equiv \rho^\alpha(r_n) - \rho^\beta(r_n)$  at the corresponding nucleus  $n$  and is given by<sup>23</sup>

$$a_{\text{iso}}^n = \frac{4\pi}{3} \beta_e \beta_n g_n \langle S_z \rangle^{-1} \sum_{\mu, \nu} P_{\mu\nu}^{\alpha-\beta} \langle \varphi_\mu(r_{kn}) | \delta(r_{kn}) | \varphi_\nu(r_{kn}) \rangle \quad (3)$$

where  $P_{\mu\nu}^{\alpha-\beta}$  is a spin-density matrix element.

Two principal mechanisms, which contribute to  $a_{\text{iso}}$  in opposite ways, include the direct delocalization of the spin density onto  $s$ -type orbitals and spin polarization. When there is a significant involvement of metal  $s$ -orbital character in the SOMO, which leads to the dominance of its direct contribution to the spin density, reasonable agreement between the theoretical and experimental  $a_{\text{iso}}$  values was usually found.<sup>13,15</sup> However, the situation becomes more complicated when spin polarization is dominant. In such cases, the use of large basis sets, often fully uncontracted or loosely contracted, which accurately describe the spin density at the given nucleus, is essential for the correct prediction of the HFCC.

The anisotropic part,  $\mathbf{T}^n$ , of the hyperfine tensor reflects the asymmetry of the spin density about each nucleus of interest. The coupling between the unpaired electron and nuclear spins

is a dipole–dipole interaction. To first order, it can be calculated from the following equation:<sup>24</sup>

$$T_{ij}^n = \frac{1}{2} g_e \beta_n g_n \langle S_z \rangle^{-1} \sum_{\mu, \nu} P_{\mu\nu}^{\alpha-\beta} \langle \varphi_\mu(r_{kn}) | r_{kn}^{-5} (r_{kn}^2 \delta_{ij} - 3r_{kn,i} r_{kn,j}) | \varphi_\nu(r_{kn}) \rangle \quad (4)$$

It has been reported that calculations of the anisotropic hyperfine constants are rather insensitive to the method that is used<sup>7,25,26</sup> because this interaction depends on the whole spatial distribution of the spin density, as opposed to the spin density at the nucleus that gauges the isotropic component, but such statements should be taken with some caution.

Zeolite centers hosting the copper cations were modeled with a five-membered  $[\text{Si}_4\text{AlO}_5(\text{OH})_{10}]^-$  cluster (truncated M7 site) and a smaller three-membered  $[\text{Si}_2\text{AlO}_2(\text{OH})_8]^-$  cluster (I2 site) that was cut off from the MFI structure as described elsewhere in detail.<sup>27</sup> Their spatial locations and structural relations with respect to the MFI framework are shown in Figure 1. For the geometry optimization, we employed a self-consistent Kohn–Sham formalism implemented in DMol code<sup>28</sup> assuming  $C_1$  symmetry for the entire cluster. The calculations were carried out within an unrestricted formalism. Thus, while discussing electronic properties we will use the terms SOMO and LUMO in the sense of the highest occupied and the lowest unoccupied spin orbitals in the spin majority manifold, respectively. As the exchange–correlation potential, we used the standard local spin-density approximation (LSDA) with the Vosko, Wilk, and Nusair exchange–correlation functional<sup>29</sup> as well as the generalized gradient approximation of Becke<sup>30</sup>–Perdew.<sup>31</sup> A double numerical basis set supplemented by polarization functions (DNP), comparable to the double- $\zeta$  plus polarization set, was used. The exchange–correlation potential was numerically integrated on a density-adjustable grid of fine quality. Charge distribution was obtained from Hirshfeld population analysis,<sup>32</sup> which is recommended for numerical DFT calculations.

Structure optimization was carried out with constraints imposed on the positions of the terminating hydrogen atoms, which were fixed at the points corresponding to the MFI lattice (geometrical embedding). Such a procedure allowed us to take into account both the local flexibility of the cluster and the simultaneous rigidity of the outer part of the zeolitic framework. Although physically less adequate than electronic or mechanical embedding, this procedure seems quite reasonable because it has recently been shown that the local structure of the Cu sites and the nitrosyl complex exhibits a rather weak dependence on the size of the cluster and the inclusion of the Madelung potential.<sup>33</sup>

Single-point calculations of HFCCs were performed with the Gaussian 98 program<sup>34</sup> for the optimized structures of both  $\eta^1\{\text{CuNO}\}^{11}[\text{Si}_2\text{AlO}_2(\text{OH})_8]$  and  $\eta^1\{\text{CuNO}\}^{11}[\text{Si}_4\text{AlO}_5(\text{OH})_{10}]$  complexes. Various combinations of different basis sets and exchange–correlation functionals  $\nu_{\text{xc}}[\rho]$  including LSDA (SVWN), generalized-gradient approximations (BLYP, BP86, BPW91), and hybrid potentials (B3PW91, B3LYP, and half-and-half-type B3LYP and B3PW91), all as implemented in Gaussian 98, were applied to establish the results as a benchmark. To reduce the number of variables to be compared with those in the experiment (a total of eight components of the  $\mathbf{A}^{\text{N}}$  and  $\mathbf{A}^{\text{Cu}}$  tensors), the calculated HFCC parameters were translated into the corresponding spin densities (determined from the Mulliken population analysis) accumulated on the Cu and N atoms using the parametrization given by Rieger<sup>35</sup> and Bowker et al.,<sup>36</sup> respectively. Taking into account the large size of the cluster,

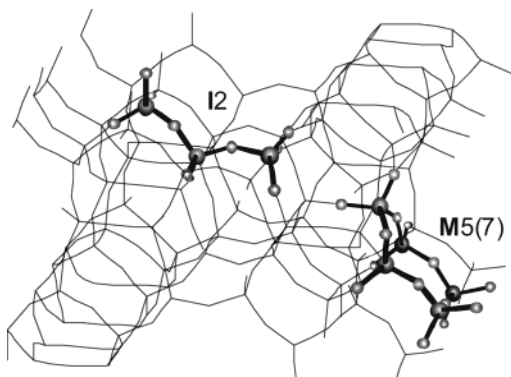


**Figure 1.** Definitions of I2 and M5(7) sites and their localization in the ZSM-5 framework (view at the (010) pentasil layer). The site denoted M5(7) is located in the wall of the main channel, and the I(2) site is in the intersection of the main and zigzag channels.

**TABLE 1: Atomic Spin Density ( $\Sigma|\rho|$ ) Distribution within the  $\eta^1\{\text{CuNO}\}^{11}$  Moiety Embedded in the  $[\text{Si}_4\text{AlO}_5(\text{OH})_{10}]^-$  Site—A Comparison of the DFT and EPR Results<sup>a</sup>**

	$\text{Cu}_\rho$	$\text{N}_\rho$	$\text{O}_\rho$	ref
EPR	0.16	0.54	$\sim 0.3$	2
VWN	0.120	0.581	0.351	this work
B88P	0.129	0.564	0.356	this work

<sup>a</sup> Atomic values of  $A^\circ_{\text{iso}}$  and  $B^\circ_{\text{aniso}}$  for  $^{63}\text{Cu}$  were calculated from ref 35, and those for  $^{14}\text{N}$  were taken from ref 36.

such a treatment seems to provide a reasonable compromise between the computational accuracy and the associated time costs.

### 3. Results and Discussion

**Experimental HFCC Parameters.** The EPR spectrum of the  $\eta^1\{\text{CuNO}\}^{11}$  adduct with well-resolved  $^{63,65}\text{Cu}$  ( $I = 3/2$ ) and  $^{14}\text{N}$  ( $I = 1$ ) hyperfine splittings was reported and fully interpreted in a previous paper<sup>2</sup>. It could be simulated only by assuming monoclinic symmetry with  $g_x = 1.999$ ,  $g_y = 2.003$ ,  $g_z = 1.889$ ,  $A^{\text{Cu}}_x = 16$  mT,  $A^{\text{Cu}}_y = 15.5$  mT,  $A^{\text{Cu}}_z = 20.5$  mT,  $A^{\text{N}}_x = 3.0$  mT,  $A^{\text{N}}_y = 0.43$  mT,  $A^{\text{N}}_z = 0.55$  mT and the noncoincidence angle  $\beta = 40^\circ$ . According to eq 2, the  $A^{\text{Cu}}$  and  $A^{\text{N}}$  tensors were decomposed as follows:

$$A^{\text{Cu}}/\text{cm}^{-1} = [149.5, 144.9, 181.8] \times 10^{-4} = \\ 158.5 \times 10^{-4} + [-9, -13.6, 22.6] \times 10^{-4} \\ A^{\text{N}}/\text{cm}^{-1} = [28, 4.0, 4.94] \times 10^{-4} = \\ 12.3 \times 10^{-4} + [15.7, -8.3, -7.4] \times 10^{-4}$$

From the molecular interpretation of these parameters, it was inferred that  $\eta^1\{\text{CuNO}\}^{11}$  is a bent adduct ( $\alpha = 160^\circ$ ) of  $C_s$  symmetry in which copper remains formally monovalent, and the NO moiety bears most of the spin density. The repartition of the spin density over copper, nitrogen, and oxygen atoms determined from the molecular interpretation of the hyperfine parameters is recollected in the first row of Table 1.

**Molecular Geometry and Electronic Structure of the  $\eta^1\{\text{CuNO}\}^{11}$  Adducts.** The structure of the ZSM-5 zeolite, illustrated in Figure 1, exhibits interconnecting straight ( $5.3 \times 5.6$  Å) and sinusoidal ( $5.1 \times 5.5$  Å) channels with a small number of nearly randomly distributed Al atoms in 12 (or 24) independent T sites in the orthorhombic (or monoclinic) polymorph.<sup>37</sup> The coordination and location of copper ions in ZSM-5 was previously investigated in detail using static lattice simulation<sup>38</sup> and combined quantum mechanics/interatomic

potential function (QM-pot) techniques.<sup>39</sup> In the case of samples with low copper content,  $\text{Cu}^+$  ions can be accommodated within the main channels (five- and six-membered M5 and M6 sites or composed M7 sites) and in the sinusoidal channels (four-, five-, and six-membered sites Z4, Z5, and Z6) as well as within the intersection of both types of channels (I2 and I3 sites, where  $\text{Cu}^+$  ions are coordinated to two or three oxygen atoms of an  $\text{AlO}_4$  tetrahedron, respectively).<sup>39</sup> The coordination and binding energy of  $\text{Cu}^+$  hosted in a given ring depend on the particular locations of the Al atoms. Among them, the I2 (with Al at the T6 position) and M7 (with Al in the T1 or T2 position) sites were found to be the most stable and could be identified with copper structures inferred from the experimental investigations using EXAFS, EPR, IR, and UV-vis techniques.<sup>40,41</sup>

The M7 site located at the main channel comprises two joint five-membered rings where three out of seven T atoms are common and can therefore be considered to be a more robust version of the simpler five-membered centers (M5, Z5). The distinctly smaller I2 site protruding into the intersection of the main and sinusoidal channels consists of a central  $\text{AlO}_4$  surrounded by two  $\text{SiO}_4$  tetrahedra terminated by OH groups. Guided by the work of Sauer et al.,<sup>39,42</sup> these sites were taken in our calculations as two generic centers for hosting the  $\text{Cu}^+$  ions. The I2-type center was modeled using a  $[\text{Si}_2\text{AlO}_2(\text{OH})_8]^-$  cluster with the Al atom placed in the T6 position. Despite being rather rudimentary, this cluster was extensively used to investigate the electronic and molecular structure of various TMI hosted in zeolites and their interactions with small molecules such as NO and  $\text{NO}_2$ .<sup>43–45</sup> As the epitome of the M7 site, we have used a simpler model containing only five T atoms instead of seven. Such a truncation can be justified by the fact that the  $\text{Cu}^+$  ion, located in the vicinity of the Al atom, is highly confined to only one of the twin five-membered rings.<sup>46</sup> Furthermore, the M5 cluster was successfully used in the modeling of  $\text{CuZSM-5}$  and its interaction with  $\text{NO}^{45}$  and  $\text{H}_2\text{O}^{47}$  because it provides a reasonable balance between the computational efficiency and the accuracy.<sup>33</sup> In our calculations, this site was epitomized by the  $[\text{Si}_4\text{AlO}_5(\text{OH})_{10}]^-$  cluster with Al in the T1 position, and hereafter it is labeled as M5(7).

The structure of the  $\text{Cu}[\text{Si}_2\text{AlO}_2(\text{OH})_8]$  cluster optimized at the VWN level is shown in Figure 2a, and selected geometrical parameters are summarized in Table 2. In assigning the coordination number, we have considered the  $\text{Cu}^+$  ion to be coordinated to a framework oxygen when the  $\text{Cu}-\text{O}$  bond length is  $d_{\text{Cu}-\text{O}} < 2.5$  Å.<sup>39</sup> The symmetric two-fold coordination of the  $\text{Cu}^+$  ion exhibited nearly equal  $\text{Cu}-\text{O}_z$  bond lengths ( $\langle d_{\text{Cu}-\text{O}} \rangle = 1.953$  Å), and  $\angle \text{O}_z\text{CuO}_z$  was equal to  $98^\circ$ . As expected, on passing to the nonlocal exchange-correlation functional (B88P) the  $\text{Cu}-\text{O}$  distances increased slightly ( $\langle d_{\text{Cu}-\text{O}} \rangle = 2.029$  Å) because it is well documented that LSDA tends to underestimate the bond lengths systematically.<sup>48</sup> The geometrical parameters remained in good agreement with the results of earlier calculations.<sup>39,42</sup> The coordination of an NO molecule to copper was exoenergetic by  $-34.7$  kcal/mol at the LSDA level with perturbative a posteriori GGA corrections to the total energy, and it led to a bent  $\eta^1$  adduct (the  $\text{Cu}-\text{N}-\text{O}$  angle  $\alpha = 148^\circ$ ) with a  $\text{Cu}-\text{N}$  bond length  $d_{\text{Cu}-\text{N}} = 1.738$  Å. The concomitant slight deformation of the Cu bonding to the framework consisted mainly of an appreciable contraction of the  $\text{O}_z-\text{Cu}-\text{O}_z$  angle to  $89^\circ$ , but the average  $\text{Cu}-\text{O}_z$  distance remained practically the same ( $\langle d_{\text{Cu}-\text{O}} \rangle = 1.974$  Å).

In contrast to  $\text{Cu}[\text{Si}_2\text{AlO}_2(\text{OH})_8]$ , copper ions nested in the more robust  $[\text{Si}_4\text{AlO}_5(\text{OH})_{10}]^-$  cluster exhibited an asymmetric trigonal coordination making two longer ( $\langle d_{\text{Cu}-\text{O}} \rangle = 2.036$  Å)

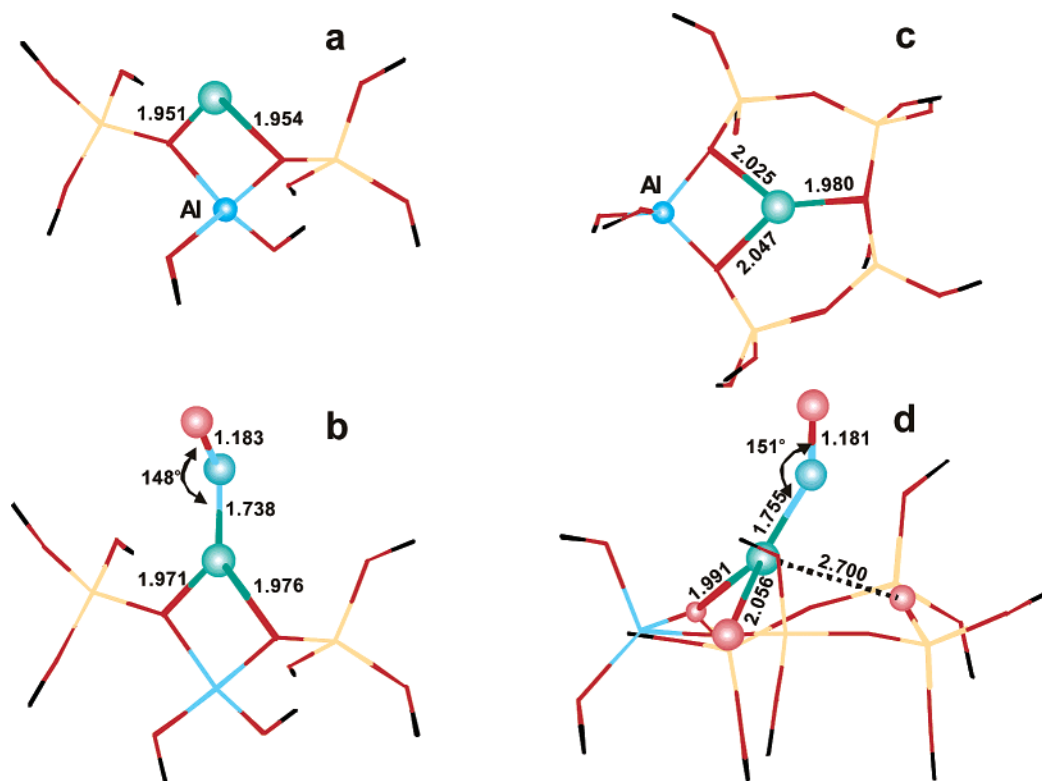


**Figure 2.** Optimized geometry (VWN) of the  $\text{Cu}^{\text{I}}/\text{I}_2$  (a),  $\eta^1\text{-N}\{\text{CuNO}\}^{\text{II}}/\text{I}_2$  (b),  $\text{Cu}^{\text{I}}/\text{M5}(7)$  (c), and  $\eta^1\text{-N}\{\text{CuNO}\}^{\text{II}}/\text{M5}(7)$  (d) complexes. The bond lengths are expressed in angstroms, and the angles, in degrees. The dashed line indicates the bond length to a distal skeletal oxygen atom.

**TABLE 2: Selected Geometric Parameters and Hirshfeld Charges for  $\text{Cu}^{\text{I}}/\text{M5}(7)$  and  $\text{Cu}^{\text{I}}/\text{I}_2$  Clusters and the Corresponding Nitrosyl Adducts in the Local Density and Generalized-Gradient Approximations**

Bond Lengths/Å								
complex	LSDA-VWN				GGA-B88P			
	$\text{Cu}^{\text{I}}/\text{I}_2$	$\text{Cu}^{\text{I}}\text{NO}/\text{I}_2$	$\text{Cu}^{\text{I}}/\text{M5}$	$\text{Cu}^{\text{I}}\text{NO}/\text{M5}$	$\text{Cu}^{\text{I}}/\text{I}_2$	$\text{Cu}^{\text{I}}\text{NO}/\text{I}_2$	$\text{Cu}^{\text{I}}/\text{M5}$	$\text{Cu}^{\text{I}}\text{NO}/\text{M5}$
Cu–O	1.951/1.95	1.971/1.97	2.025/2.047/1.98	1.991/2.05	2.024/2.03	2.030/2.04	2.065/2.145/2.04	2.044/2.14
	4	6	0	6	4	8	3	1
Cu–N		1.738		1.755		1.797		1.817
N–O		1.183		1.181		1.194		1.192
Angles/deg								
complex	LSDA-VWN				GGA-B88P			
	$\text{Cu}^{\text{I}}/\text{I}_2$	$\text{Cu}^{\text{I}}\text{NO}/\text{I}_2$	$\text{Cu}^{\text{I}}/\text{M5}$	$\text{Cu}^{\text{I}}\text{NO}/\text{M5}$	$\text{Cu}^{\text{I}}/\text{I}_2$	$\text{Cu}^{\text{I}}\text{NO}/\text{I}_2$	$\text{Cu}^{\text{I}}/\text{M5}$	$\text{Cu}^{\text{I}}\text{NO}/\text{M5}$
Cu–N–O		148		151		141		138
$\text{O}_z\text{-Cu-O}_z$	98	89	84/136/134	81	93	87	84/131/132	81
Atomic Charges								
complex	LSDA-VWN				GGA-B88P			
	$\text{Cu}^{\text{I}}/\text{I}_2$	$\text{Cu}^{\text{I}}\text{NO}/\text{I}_2$	$\text{Cu}^{\text{I}}/\text{M5}$	$\text{Cu}^{\text{I}}\text{NO}/\text{M5}$	$\text{Cu}^{\text{I}}/\text{I}_2$	$\text{Cu}^{\text{I}}\text{NO}/\text{I}_2$	$\text{Cu}^{\text{I}}/\text{M5}$	$\text{Cu}^{\text{I}}\text{NO}/\text{M5}$
Cu	0.388	0.385	0.299	0.381	0.402	0.388	0.312	0.379
N		−0.022		0.0		−0.014		0.007
O		−0.024		−0.020		−0.016		−0.010

bonds with both  $\text{O}_z\{\text{Al}, \text{Si}\}$  atoms adjacent to Al and a slightly shorter bond ( $d_{\text{Cu-O}} = 1.980 \text{ Å}$ ) with the oxygen  $\text{O}_z\{\text{Si}\}_2$  located opposite to the Al position (Figure 2c). The resultant complex was nearly planar, as could be inferred from the sum of the  $\text{O}_z\text{-Cu-O}_z$  angles equal to  $354^\circ$ .

The calculations showed that the ligation of NO ( $\Delta E_{\text{ads}} = -22.2 \text{ kcal/mol}$ ) occurred with the conservation of the total coordination number of copper as the new Cu–N link was formed at the expense of the former Cu– $\text{O}_z\{\text{Si}\}_2$  bond. The distance to the  $\text{O}_z\{\text{Si}\}_2$  atom was too large ( $2.701 \text{ Å}$ ) to satisfy the ligation condition (Figure 2d). Thus, the bound NO appears to be a powerful ligand that can dominate the coordination

sphere of copper by exerting sufficient cis influence to remove the oxygen ligand from the inner sphere of the  $\text{Cu}^{\text{I}}$  ion. The optimized geometry of the  $\eta^1\{\text{CuNO}\}^{\text{II}}$  moiety in the  $[\text{Si}_4\text{AlO}_5(\text{OH})_{10}]^-$  host in the doublet state (VWN/DNP) was close to that observed in the tritetrahedral cluster (**I2**). The copper ion formed a distorted trigonal complex ( $\Sigma \angle \text{OCuO}(\text{N}) = 358^\circ$ ) characterized by two longer ( $1.991$  and  $2.056 \text{ Å}$ ) bonds with the  $\text{O}_z\{\text{Al}, \text{Si}\}$  atoms, a distinctly shorter Cu–N bond of  $1.755 \text{ Å}$ , and a Cu–N–O angle  $\alpha = 151^\circ$  (Figure 2d). The latter was close to that assessed experimentally from the molecular analysis of the EPR data (vide supra). The structure of the NO–Cu–( $\text{O}_z$ )<sub>2</sub> unit exhibited nearly  $C_s$  microsymmetry with the mirror



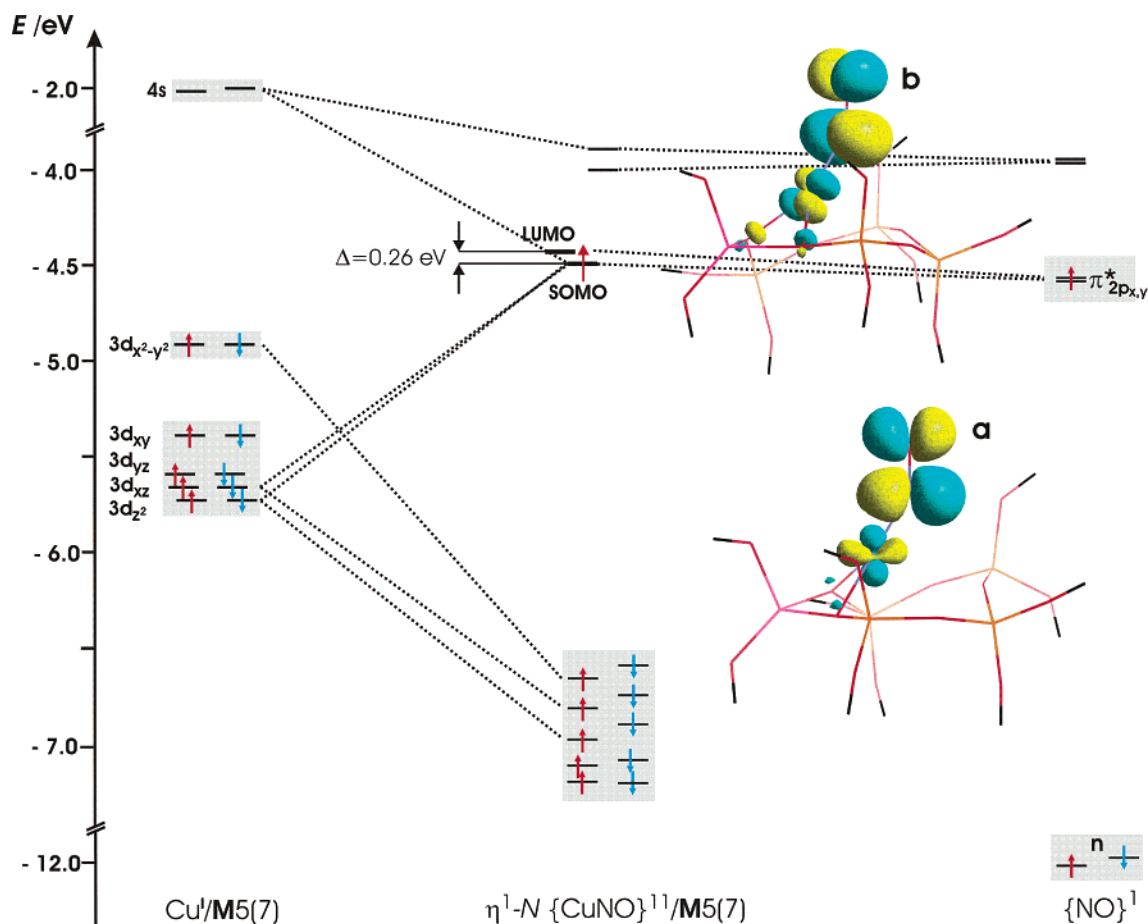


**Figure 3.** Kohn–Sham molecular correlation diagram of principal spin orbitals involved in the formation of the bond between the  $\text{Cu}^+/\text{M5(7)}$  site and the NO molecule. Bending of the adduct results in the splitting of both  $2\pi_g^*$  levels, giving rise to the SOMO (a) and LUMO (b).

plane (containing Cu, N, and the distal  $\text{O}_z\{\text{Si}\}_2$  atom) bisecting the  $\delta_{\text{O}-\text{Cu}-\text{O}}$  angle defined by the bonds between Cu and the both proximal  $\text{O}_z\{\text{Al}, \text{Si}\}$  atoms. The departure of the NO ligand from this plane was smaller than  $6^\circ$ . The tilting of NO toward the shorter  $\text{Cu}-\text{O}_z\{\text{Al}, \text{Si}\}$  bonds is a rather general phenomenon and has been previously observed (e.g., by Scheidt and Ellison for  $\{\text{FeNO}\}^7$  species) and interpreted in terms of an increased  $d_{z^2}-2\pi^*$  NO interaction.<sup>49</sup>

The adsorption of nitric oxide led to the partial oxidation of copper; for the  $\eta^1\{\text{CuNO}\}^{11}/\text{M5(7)}$  adduct,  $\Delta Q_{\text{Cu}} = +0.08$ , but in the case of  $\eta^1\{\text{CuNO}\}^{11}/\text{I2}$ , one copper oxidation state remained practically unchanged ( $\Delta Q_{\text{Cu}} \approx 0.00$ ). A parallel reduction of the NO ligand ( $\Delta Q_{\text{NO}} = -0.02$  and  $-0.05$  for **M5(7)** and **I2**, respectively) was simultaneously observed. This indicated that  $\pi$  back-donation, manifested also in the N–O bond lengthening ( $\Delta d_{\text{N}-\text{O}} \approx 0.03$  Å in comparison to that of gaseous NO), dominated  $\sigma$  donation, leading to a nitroside-type of activation of the nitric oxide (formation of bound  $\text{NO}^{\delta-}$ ). Consequently, the calculated NO stretching frequencies equal to  $1820\text{ cm}^{-1}$  for **M5(7)** and  $1813\text{ cm}^{-1}$  for **I2**, which agree well with the experimental frequency ( $1809\text{ cm}^{-1}$ ),<sup>27</sup> were downshifted with respect to the corresponding calculated free NO(g) value ( $1910\text{ cm}^{-1}$ ).

The binding of NO to copper caged in ZSM-5 imparts unique properties both to the metal center and the nitrosyl ligand itself, which are manifested in the reactivity and unusual magnetic properties of the resultant adduct.<sup>2,27</sup> Insight into the electronic structure of the Cu–NO bond was inferred from the analysis of the partial DOS of the  $\eta^1\{\text{CuNO}\}^{11}/\text{M5(7)}$  complex in the vicinity of the Fermi level, which provided useful hints

concerning the constitution of the frontier orbitals. The analysis showed that this region was dominated by a large contribution from the nitrogen  $2p_{x,y}$  orbitals complemented by a small fraction of  $2s$  and  $2p_z$  orbitals (57% in total) and  $2p_{x,y}$  oxygen orbitals (34%) along with considerable copper  $4s$ ,  $3d_{z^2}$  and  $3d_{xz,yz}$  character (11%).

The partitioning of the total DOS helped us to track down a simplified Kohn–Sham molecular spin-orbital diagram for NO ligation to the  $\text{Cu}^+/\text{M5(7)}$  ion (Figure 3). The nitrosyl group was reduced to its essentials: the low-lying ( $E_n \approx -11.9$  eV) lone pair  $n$  ( $s + p_z$  hybrid) and the high-lying degenerate  $2\pi^*$  levels ( $E_{\pi^*} \approx -4.8$  eV), situated close to the d manifold of copper ( $E_{3d} \approx -5.7/-4.9$  eV). This indicated that the NO ligand is prone to act as a stronger  $\pi$  acceptor than  $\sigma$  donor.

The bond between the closed-shell  $\text{Cu}^+$  ( $1S$ ) and the NO radical ( $^2\Pi$ ) can be rationalized in terms of the  $s/d$  hybridization of the empty  $4s$  ( $E_{4s} = -2.011$  eV) and two occupied  $3d_\sigma$  orbitals:  $3d_{z^2}$  ( $E_{3d_{z^2}} = -5.735$  eV) and  $3d_{xz}$  ( $E_{3d_{xz}} = -5.600$  eV) of the copper center discussed earlier by Bauschlicher et al.<sup>50</sup> The unoccupied  $3d_{z^2} + 4s$  acceptor hybrid exhibiting an improved spatial spread along the bond axis can overlap more efficiently with the in-plane  $\pi_g^x$  of NO, and the interaction of the lone pair  $n$  is weaker because the latter is situated rather low in energy. Such an interaction provides a pathway for the  $\sigma$ -type bond producing the SOMO ( $E_{\text{SOMO}} = -4.551$  eV). Correlating the occupied  $3d_{yz}$  orbital with the remaining out-of-plane empty  $\pi_g^y$  gives rise to the LUMO ( $E_{\text{LUMO}} = -4.295$  eV), in accordance with the empirical binding scheme devised from the earlier EPR investigations.<sup>2</sup> Both frontier orbitals are antibonding between the metal and the ligand and exhibit mixed

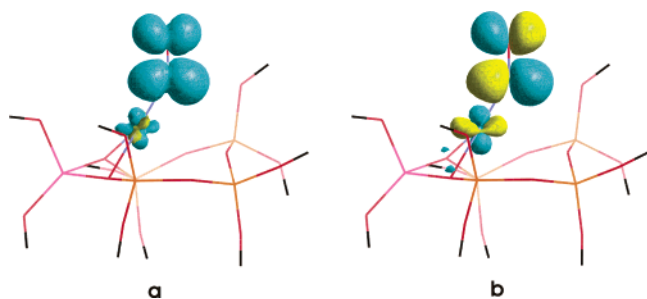


**Figure 4.** (a) Spin-density contour ( $\rho^\alpha(r_n) - \rho^\beta(r_n)$ ) and (b) the SOMO calculated at the BPW91/LanL2DZ level for the  $\eta^1\{\text{CuNO}\}^{11}[\text{Si}_4\text{AlO}_5(\text{OH})_{10}]$  complex.

$2\pi_g$ -3d character with a dominant NO component. The resulting charge redistribution within the Cu-NO moiety results in the partial oxidation of copper and the consequent reduction of the NO ligand, as described above.

The lowering of the symmetry upon coordination in the bent  $\eta^1$  fashion gives rise to a splitting of the perturbed  $2\pi_g$  levels by the amount  $\Delta_{\text{DFT}} = 0.26$  eV, which compares well with  $\Delta_{\text{EPR}} = 0.24$  eV deduced previously from the  $g$ -tensor analysis.<sup>2</sup> Except for the already mentioned  $3d_{z^2}-2\pi_g^x$  interaction, the driving force for bending is reinforced by an improved overlap between  $2\pi_g^x$  with 4s, which is not allowed in the linear mode of the NO ligation.

The spin-density contour of the  $\eta^1\{\text{CuNO}\}^{11}[\text{Si}_4\text{AlO}_5(\text{OH})_{10}]$  adduct (Figure 4), calculated at the BPW91/LanL2DZ level (vide infra), shows that it is mainly localized on the NO ligand (about a half share on the nitrogen atom) with a sizable copper contribution. Interestingly, it is practically confined to the CuNO moiety. Thus, for conventional classification purposes, the intrazeolite copper nitrosyl can be treated as a ligand-centered  $[\text{Cu}^{1-2}(\cdot\text{N}=\text{O})]$  radical.

Comparing the spin-density plot with the SOMO (Figure 4a and b) revealed that there is noticeable spin polarization of the copper orbitals that modifies the spin-density distribution with respect to that derived from the unpaired electron density. It is particularly pertinent to the out-of-plane  $3d_{yz}$  orbital, which acquires a negative spin density, thereby influencing the calculated dipolar tensor. A similar discrepancy between the plots of spin and unpaired electron densities was observed previously for the  $\text{CpCo}(\text{CO})_2^-$  ion, indicating that estimates of orbital populations in the SOMO from EPR data for complex transition-metal-containing systems may sometimes lead to some inconsistencies with the quantum chemical calculations because of the difficulties arising from the spin-polarization effects.<sup>14</sup>

The repartition of the spin density over Cu, N, and O atoms is summarized in Table 1 and compared with the corresponding experimental values derived from the analysis of the  $^{14}\text{N}$  hyperfine and  $^{63,65}\text{Cu}$  superhyperfine tensors. Taking into account that in the latter case, to make the problem tractable, the explicit contribution of 4p orbitals was not taken into account in the analysis (which obviously overestimates the spin density on 3d orbitals), the agreement between the experimental and calculated values is quite reasonable, except for the already-mentioned negative spin density on the  $3d_{yz}$  orbital, which was not predicted by the analysis of the experimental copper dipolar tensor.

**Calculation of HFCC: Influence of the Exchange-Correlation Functionals.** The major problem in calculating magnetic parameters is a proper description of both the core- and valence-shell spin polarization without introducing appreciable spin contamination. This has motivated us to make a detailed examination of the influence of the  $v_{xc}[\rho]$  functional on the

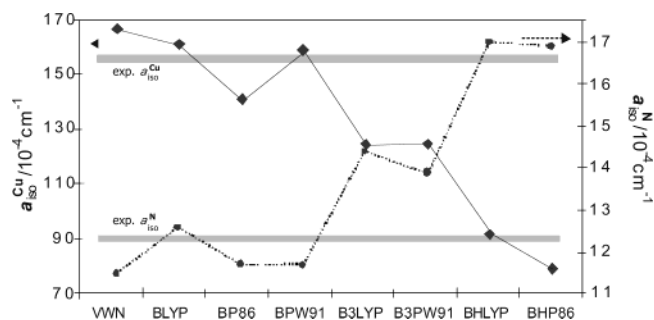


**Figure 5.** Influence of the exchange-correlation functional on the isotropic hyperfine constant  $a_{\text{iso}}$  of copper (—) and nitrogen (····) for the CuNO/M5(7) complex.

HFCC using LanL2DZ<sup>51</sup> and 6-311G(df) basis sets, which appeared to be the most suitable for this purpose. In the initial stage of the calculations, we investigated the influence of eight different LSDA, GGA, and hybrid functionals (VWN, BLYP, BP86, BPW91, B3LYP, B3PW91, BHLYP, and BHP86) on the values of nitrogen and copper isotropic constants. The results that are collated in Figure 5 reveal a strong dependence of both  $a_{\text{iso}}$  values on the electron exchange-correlation effects, and they follow opposite trends. ( $a_{\text{iso}}^{\text{N}}$  was calculated using the LanL2DZ basis set, whereas  $a_{\text{iso}}^{\text{Cu}}$  was obtained with 6-311G(df) because it was not accessible within the pseudopotential scheme.) For the most unfavorable combinations of the half-and-half  $v_{xc}$  (BHLYP and BHP86), the discrepancy between the calculated and experimental values reached the level of 50%, but it was lower than 10% (either for copper or nitrogen  $a_{\text{iso}}$ ) in the case of the BLYP and BPW91 functionals. Generally, the dependence on  $v_x[\rho]$  dominated that on  $v_c[\rho]$ . For a given exchange functional  $v_x[\rho]$ , the Fermi contact term of copper varied with the correlation functional  $v_c[\rho]$  as  $a_{\text{iso}}^{\text{Cu}}(\text{LYP}) \geq a_{\text{iso}}^{\text{Cu}}(\text{PW91}) > a_{\text{iso}}^{\text{Cu}}(\text{P86})$ , and for a given correlation functional,  $a_{\text{iso}}^{\text{Cu}}$  decreased with  $v_x[\rho]$  in the series  $a_{\text{iso}}^{\text{Cu}}(\text{B}) > a_{\text{iso}}^{\text{Cu}}(\text{B3}) > a_{\text{iso}}^{\text{Cu}}(\text{BH})$ . Apparently, the computed spin density at the copper nucleus was reduced when the exact exchange had been augmented, whereas in the case of nitrogen the opposite trend was observed. This can be associated with different physical origins of both  $a_{\text{iso}}$  values. Whereas for nitrogen it is primarily due to spin polarization, in the case of copper the isotropic HFCC is more complex in nature because it results from direct (delocalization) and indirect (polarization) effects, which being of opposite sign mutually cancel. Because the unrestricted Hartree-Fock wave functions are known to overestimate spin polarization,<sup>52</sup> it is then quite reasonable that an enhanced exact exchange decreased the value of  $^{\text{Cu}}a_{\text{iso}}$ , which is discussed in the next paragraph.

The dipolar coupling calculation can provide further direction concerning the choice of optimal  $v_{xc}$ . Following Manzarova and Kaupp,<sup>13</sup> we have chosen the total spin density ( $\sum |\rho_i|$ ) on copper 3d and nitrogen 2p orbitals to be two concise ancillary parameters suitable for testing the performance of different functionals in relation to their potential usefulness in the computation of the anisotropic part of the HFCCs. The results shown in Figure 6 indicate that the calculations generally tend to overestimate the experimental values. The variation of  $\rho_{\text{Cu}}$  and  $\rho_{\text{N}}$  with  $v_{xc}[\rho]$  followed the opposite trend,  $\rho_{3d}$  on copper decreased whereas  $\rho_{2p}$  on nitrogen was enhanced with the increase in the exact exchange. Although the overall range of the changes for Cu and N was different, in both cases the extreme results varied by no more than 20%. Once more, the dependence on  $v_x[\rho]$  dominated that on  $v_c[\rho]$ . From the inspection of Figure 6, it was inferred that for a given exchange

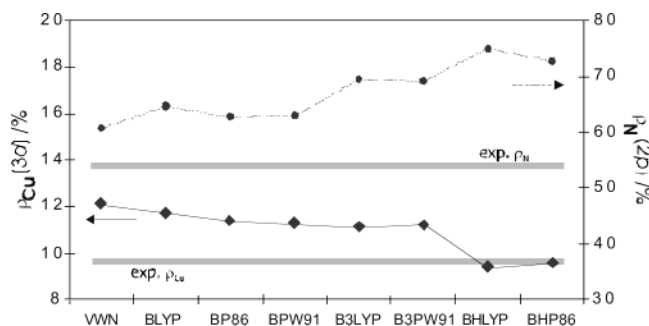


**Figure 6.** Dependence of the spin density  $\rho_{\text{Cu}}$  on copper 3d (—) and  $\rho_{\text{N}}$  on nitrogen 2p orbitals (···) as a function of the exchange-correlation functional for the  $\text{Cu}^1\text{NO}/\text{M5}(7)$  complex.

functional  $v_x[\rho]$  the computed 3d spin density on copper varied with the correlation functional  $v_c[\rho]$  as  $\rho_{\text{Cu}}(\text{LYP}) \geq \rho_{\text{Cu}}(\text{P86}) \geq \rho_{\text{Cu}}(\text{PW91})$ , and for a given correlation functional,  $\rho_{\text{Cu}}$  decreased with  $v_x[\rho]$  in the series  $\rho_{\text{Cu}}(\text{B}) \approx \rho_{\text{Cu}}(\text{B3}) > \rho_{\text{Cu}}(\text{BH})$ . The spin density on copper seems to be reduced with the inclusion of exact exchange approaching the experimental value for BHLYP and BHP86. The latter trend was accompanied by a simultaneous enhancement of the spin density on the nitrogen atom. Thus, the increasing admixture of exact exchange shifted the spin density from Cu to the NO ligand. (A similar effect was previously described for  $\text{CuO}$ .<sup>13</sup>) As a result, in the case of the hybrid BH functionals with 50% exact exchange, good agreement with the experimental value of  $\rho_{\text{Cu}}$  was achieved, unfortunately at the expense of  $\rho_{\text{N}}$  accuracy.

The 2p spin density on nitrogen depended on  $v_c[\rho]$  as  $\rho_{\text{N}}(\text{LYP}) > \rho_{\text{N}}(\text{P86}) \approx \rho_{\text{N}}(\text{PW91})$  for a given  $v_x[\rho]$  and  $\rho_{\text{N}}(\text{BH}) > \rho_{\text{N}}(\text{B3}) > \rho_{\text{N}}(\text{B})$  for a given  $v_c[\rho]$  functional. The observed changes can be traced to the impact of the exchange-correlation effects on the spin polarization of the valence shell but also to the modification of the SOMO shape. With the introduction of the HF exchange from LSDA through pure GGA to hybrid and half-and-half functionals, the contribution of spin polarization to  $\rho_{\text{N}}$  is expected to increase. However, this effect could be an artifact because, as already mentioned, UHF overestimates spin polarization, leading to spin contamination. The latter effect was found to vary from  $\langle S^2 \rangle = 0.7546$  (for SVWN) to 0.7795 (for BHLYP).

Even from the first inspection of Figures 5 and 6, it is clear that it was not possible to select one functional that would be superior to others. Reasonable results could be obtained with any of the GGA functionals, whereas the hybrids were evidently less successful. These calculations did not take into account a second-order contribution to  $a_{\text{iso}}$  arising from spin-orbit coupling because the latter is not included in Gaussian 98. The influence of the corresponding pseudocontact term discussed below in more detail (eq 5) shows that it has the opposite effect on  $a_{\text{iso}}$  with respect to exact exchange. Thus, the good performance of GGA functionals could be related to the cancellation of errors. It may be worth noting that for copper oxide Kaupp et al.<sup>13</sup> have also found that GGA calculations give better results than the hybrid calculations. Therefore, for further investigations, we selected an apparently most advantageous BPW91 functional and, for the sake of comparison, also the popular B3LYP (which includes ca. 20% of HF exchange) to examine the influence of enhanced exact exchange on HFCCs.

**Influence of the Basis Set.** The ability of the DFT calculations to reproduce HFCCs correctly depends essentially upon a suitable choice of basis sets.<sup>13–15</sup> Whereas for the light main-group atoms the basis set dependence of the hyperfine parameters has already been discussed in detail, systematic studies

have been reported only for small transition-metal-containing systems.<sup>13</sup> It is found that because of the error compensation smaller basis sets often compare quite well with the largest one. This effect seems to be systematic rather than accidental, implying the usefulness of smaller basis sets for application to large systems.<sup>13</sup>

In our computational approach to HFCCs, the first round of calculations was carried out on a minimal triatomic  $\{\text{CuNO}\}^{11}$  system to select the optimal basis set/functional combinations for further work with more adequate larger clusters. The performance of various 6-31G and 6-311G basis sets augmented by polarization and diffuse functions (three sets of  $d$  functions and one set of  $f$  functions), ECP-type basis sets (LanL2MB, LanL2DZ, SDD, CEP-121G), and split-valence-type basis sets (SV, SVP, TZV) was investigated in turn. The results obtained with the 6-31G basis sets were not convergent; therefore, this group was rejected. Among the ECP and split-valence basis sets, LanL2DZ and TZV appeared to be as good as the augmented 6-311G-type functions. However, the more robust mixed basis sets (6-311G(3df) for Cu, EPR-II, and EPR-III; cc-pVnZ for N and O atoms) gave results similar to those obtained with the less-demanding bases of 6-311G and the ECP type. As a result, for further investigations we have selected the family of 6-311G and LanL2DZ basis sets.

The HFCCs for  $^{63}\text{Cu}$ ,  $^{14}\text{N}$ , and  $^{17}\text{O}$  nuclei obtained with B3LYP and BPW91 functionals are summarized in Table 3 and compared with the available experimental data. Unfortunately, for  $^{17}\text{O}$  they are not available yet, but the calculations can provide some useful supporting information for future EPR studies concerning the sign, magnitude, and orientation of the oxygen-17 hyperfine tensor. In the last column of Table 3, the  $\langle S^2 \rangle$  values are included as a convenient measure of the spin contamination due to the unrestricted type of calculations. Because they were all close to 0.75, the contamination was rather minor, indicating the good overall quality of the wave functions used in the calculations. Generally, the best results were obtained by combining the BPW91 functional with LanL2DZ basis sets. As expected, the  $^{14}\text{N}$  hyperfine tensor was reproduced more accurately than the  $^{63}\text{Cu}$  superhyperfine tensor. The calculations confirmed the choice of the signs adopted in the previous analysis of the EPR data and the general features of the experimental SOMO. The largest deviations from the corresponding experimental values were encountered in the case of the  $T_{xx}$  component of the  $^{63}\text{Cu}$  dipolar tensor (which was too small by  $\sim 50\%$ ) and the  $T_{yy}$  component (which was too large by  $\sim 40\%$ ); however, the  $T_{zz}$  value was reproduced quite satisfactorily, taking into account that the second-order spin-orbit effects<sup>53</sup> are not included in the Gaussian 98 calculation scheme. A poor reproduction of  $T_{xx}$  and  $T_{yy}$  is most probably caused by an exaggerated polarization of the  $3d_{yz}$  orbital that determines, along with the  $3d_{xz}$  and  $3d_{z^2}$  direct contributions, the  $T^{\text{Cu}}$  tensor:

$$T_{zz} \sim \frac{2}{7} P_{\text{Cu}}(2g + h - f)$$

$$T_{yy} \sim \frac{2}{7} P_{\text{Cu}}(-g - 2h - f)$$

$$T_{xx} \sim \frac{2}{7} P_{\text{Cu}}(-g + h + 2f)$$

$P_{\text{Cu}} = 402.4 \times 10^{-4} \text{ cm}^{-1}$  for the monovalent copper, and  $g$ ,  $h$ , and  $f$  describe the share of the  $3d_{z^2}$ ,  $3d_{xz}$ , and  $3d_{yz}$  orbitals, respectively. When  $g > h \sim f$ , the parameter  $h$  may be replaced by  $f$  (or vice versa), and the  $T$  tensor assumes a simpler form



**TABLE 3: HFCC Parameters of  $^{63}\text{Cu}$ ,  $^{14}\text{N}$ , and  $^{17}\text{O}$  for Optimized  $\eta^1\{\text{CuNO}\}^{11}[\text{Si}_4\text{AlO}_5(\text{OH})_{10}]$  and  $\eta^1\{\text{CuNO}\}^{11}[\text{Si}_2\text{AlO}_2(\text{OH})_8]$  Clusters Calculated with B3LYP and BPW91 Exchange-Correlation Functionals**

basis set	$A(^{63}\text{Cu})/10^{-4} \text{ cm}^{-1}$				$A(^{14}\text{N})/10^{-4} \text{ cm}^{-1}$				$A(^{17}\text{O})/10^{-4} \text{ cm}^{-1}$				$\langle S^2 \rangle$	
	$a_{\text{iso}}$	$T_{ii}$			$a_{\text{iso}}$	$T_{ii}$			$a_{\text{iso}}$	$T_{ii}$				
$\eta^1\{\text{CuNO}\}^{11}/\text{M5(7)} \text{ B3LYP}$														
6-311G(df)	122.2	-5.7	-22.4	28.1	7.4	21.2	-10.9	-10.3	-6.5	23.0	21.9	-44.9	0.7546	
LanL2DZ		-3.3	-19.0	22.3	14.4	20.9	-10.9	-10.1	-20.2	22.9	21.0	-43.9	0.7566	
$\eta^1\{\text{CuNO}\}^{11}/\text{M5(7)} \text{ BPW91}$														
6-311G(df)	158.7	-5.4	-24.5	29.9	4.2	19.3	-9.9	-9.4	-0.1	21.6	20.5	-42.1	0.7527	
LanL2DZ		-4.1	-19.0	23.1	11.7	19.1	-9.8	-9.3	-14.4	23.1	22.6	-45.7	0.7529	
$\eta^1\{\text{CuNO}\}^{11}/\text{I2} \text{ B3LYP}$														
6-311G(df)	134.2	-5.1	-22.3	28.4	6.3	20.5	-10.5	-10.0	-6.5	23.5	22.2	-45.7	0.7542	
LanL2DZ		-2.1	-20.7	22.8	13.3	19.8	-10.3	-9.5	-21.4	24.6	19.5	-44.1	0.7611	
$\eta^1\{\text{CuNO}\}^{11}/\text{I2} \text{ BPW91}$														
6-311G(df)	168.7	-6.0	-24.7	30.7	4.1	18.9	-9.8	-9.1	-0.7	22.5	21.1	-43.7	0.7536	
LanL2DZ		-3.8	-20.4	24.2	11.3	18.1	-9.5	-8.6	-15.2	22.9	20.1	-43.0	0.7557	
EPR data	158.5	-9.0	-13.6	22.6	12.3	15.7	-8.3	-7.4					0.75	

**TABLE 4: Copper  $a_{\text{iso}}$  values for  $\eta^1\{\text{CuNO}\}^{11}/\text{M5(7)}$  and  $\eta^1\{\text{CuNO}\}^{11}/\text{I2}$  adducts Calculated with B3LYP and BPW91 Functionals Using Basis Sets of Increasing Flexibility**

method	$a_{\text{iso}}^{\text{Cu}}/10^{-4} \text{ cm}^{-1}$	
	$\eta^1\{\text{CuNO}\}^{11}/\text{M5(7)}$	$\eta^1\{\text{CuNO}\}^{11}/\text{I2}$
B3LYP/6-311G	119.1	128.5
B3LYP/6-311G(d)	124.5	147.2
B3LYP/6-311G(df)	122.2	134.2
BPW91/6-311G	147.7	160.0
BPW91/6-311G(d)	161.7	178.5
BPW91/6-311G(df)	158.7	168.7

$\{T_{zz} \sim {}^2/{}_7P(2g), T_{yy} \sim {}^2/{}_7P(-g - 3f), T_{xx} \sim {}^2/{}_7P(-g + 3f)\}$ , indicating that in such case the polarization should have little impact on the  $T_{zz}$  component, which is dominated by the large  $2g$  term, because both  $h$  and  $f$  contributions, being smaller ( $2g \gg h, f$ ), mutually cancel. It might, however, significantly influence the  $T_{yy}$  and the  $T_{xx}$  value even more (this is the principal direction of the  $f$  tensor) because now  $h$  and  $f$  act in concert versus  $g$ , making the former component larger and the latter one smaller (in terms of the absolute values) in comparison to their experimental counterparts, as observed (Table 3).

It is worth mentioning that the LanL2DZ basis set has already been reported to function quite well in calculations of many other properties of transition metals<sup>54,55</sup> because it contains relativistic pseudopotentials. Unfortunately, because the copper inner  $1s, 2s$ , and  $2p$  electrons are described by an effective core potential (ECP), this basis is not suitable for calculations of the Fermi contact term of copper. Therefore, for calculations of  $a_{\text{iso}}(\text{Cu})$ , more suitable 6-311G-type basis sets have been selected (Table 4).

The results obtained with the BPW91 functional appeared to be distinctly better than those calculated using the more highly recommended B3LYP, which clearly failed to reproduce  $a_{\text{iso}}(\text{Cu})$  correctly. For further discussion of the B3LYP performance, the isotropic superhyperfine constant of copper can be factored into the direct SOMO contribution ( $P_{\text{Cu}}\kappa_s\rho_s$ ), the spin polarization term ( $Q_d\rho_d$ ), and the pseudocontact term ( $P_{\text{Cu}}\langle\Delta g\rangle$ ):<sup>56</sup>

$$a_{\text{iso}}(\text{Cu}) = P_{\text{Cu}}\kappa_s\rho_s + Q_d\rho_d + P_{\text{Cu}}\langle\Delta g\rangle \quad (5)$$

$\kappa_s = 5.01$ , the polarization constant  $Q_d = 150 \times 10^{-4} \text{ cm}^{-1}$ , and  $\langle\Delta g\rangle = 2.0023 - {}^1/{}_3(g_{xx} + g_{yy} + g_{zz}) = 0.0386$ . Substituting these numerical values into eq 5 reveals a decreasing (by an order of magnitude) hierarchy of the importance of these terms. The pseudocontact contribution to  $a_{\text{iso}}(\text{Cu})$  is apparently too small ( $15.6 \times 10^{-4} \text{ cm}^{-1}$ ) to account for the observed difference with respect to the experiment (Table 3). If, however, the spin

polarization were responsible for poor  $a_{\text{iso}}(\text{Cu})$  reproduction, then one might expect that better accuracy could be achieved with a larger 6-311G(df) basis.

The results collated in Table 4 show that no significant improvement can be obtained in this way with the B3LYP functional. Furthermore, the observed discrepancies are too large to be caused by inaccurate calculations of the spin polarization. Indeed, compensation for the error requires an unrealistically high spin density localized on the copper 3d orbitals

$$\rho_d = (143 \times 10^{-4} \text{ cm}^{-1} - 90 \div 100 \times 10^{-4} \text{ cm}^{-1}) / 150 \times 10^{-4} \text{ cm}^{-1} = 0.35 \div 0.29$$

that would be in variance with the observed  $T$  and  $g$  tensors. Therefore, the most probable reason for the encountered difficulties in the B3LYP calculation of  $a_{\text{iso}}(\text{Cu})$  stems from the plausible underestimation of the 4s contribution to the SOMO. This parameter has to be calculated very precisely because of the high value of the  $P\kappa_s$  term ( $2016 \times 10^{-4} \text{ cm}^{-1}$ ). Thus, even a small inaccuracy caused, for example, by bond-length/angle errors translates into a substantial change in the calculated isotropic coupling constant, as inferred from our preliminary investigations of the structure sensitivity of the HFCCs. However, essential improvement was obtained upon replacing the B3LYP functional with the BPW91. Along with the enlargement of the basis to a flexible 6-311G(df), it led to a formidable agreement with  $a_{\text{iso}}(\text{Cu})$  derived from the EPR data.

Alternatively, the strength of the polarization effect may be estimated by comparing  $a_{\text{iso}}$  obtained from restricted open (RO) and unrestricted (U) schemes of the calculations. In our case, the spin-polarization term  $\Delta a_{\text{iso}}^{\text{pol}} = a_{\text{iso}}(\text{RO}) - a_{\text{iso}}(\text{U})$  was equal to  $22 \times 10^{-4} \text{ cm}^{-1}$  for BPW91 and  $38 \times 10^{-4} \text{ cm}^{-1}$  for the B3LYP functional, again indicating the exaggerated importance of spin polarization when exact exchange is included because the experimental estimate of  $a_{\text{iso}}^{\text{pol}}$  gave a value of  $15 \times 10^{-4} \text{ cm}^{-1}$  only.

Contrary to the HFCCs of copper, the calculated  $^{14}\text{N}$  and  $^{17}\text{O}$  hyperfine tensors did not significantly depend on the basis sets except for the  $a_{\text{iso}}$  component, as might be expected. Once again, the smaller LanL2DZ basis appeared to be sufficient to reproduce the  $^{14}\text{N}$  hyperfine parameters fairly. Extending the basis to double- $\zeta$  EPR-II and more sophisticated triple- $\zeta$  EPR-III (specially developed for HFCC calculations) did not improve the accuracy of the anisotropic hyperfine tensor ( $A^{\text{N}}/\text{cm}^{-1} = [22.4/-11.5/-10.9] \times 10^{-4}$ ) considerably in comparison to that obtained with the smaller LanL2DZ basis. Furthermore, a



more flexible description of the s core-shell orbitals using 6-311G(df) has reduced  $a_{\text{iso}}(\text{N})$  far below the experimental value (Table 3).

Although the calculated magnetic parameters are consistent with the following generic binding scheme of  $(\text{O}_2\{\text{Al}, \text{Si}\})_2\text{-Cu-NO}$ , there is a distinct difference in  $a_{\text{iso}}(\text{Cu})$  values obtained for I2 and M5(7) sites, with  $a_{\text{iso}}(\text{I2}) > a_{\text{iso}}(\text{M5})$ . This suggests possible speciation of the nitrosyl adducts that may be reflected in EPR spectra, provided that the resolution is sufficiently good. Indeed, recent high-field EPR work on copper nitrosyl adducts in ZSM-5 has revealed the presence of two adducts with higher and lower  $a_{\text{iso}}(\text{Cu})$  values that can be associated with these sites.<sup>4</sup>

#### 4. Conclusions

The calculations revealed that the formation of the paramagnetic  $\eta^1\{\text{CuNO}\}^{11}$  adduct occurs along the nitroside pathway. Independent of the copper site, the adduct exhibits a nearly trigonal-planar structure with the  $\eta^1\text{-N}$  bent CuNO moiety. Tilting of the adduct improves the overlap between the NO  $2\pi_g$  and Cu 4s orbitals, giving rise to a large positive value of  $a_{\text{iso}}(\text{Cu})$ . A combination of the LanL2DZ basis set with the BPW91 functional can be used as a convenient approach to the DFT estimation of HFCCs for copper-nitrosyl clusters, providing a reasonable compromise between the computational effort and the accuracy. The results of the  $^{14}\text{N}$  hyperfine and  $^{63}\text{Cu}$  superhyperfine structure calculations corroborate the experimental data and confirm the previous sign analysis of the  $A^{\text{Cu}}$  and  $A^{\text{N}}$  tensors. The redistribution of the spin density over Cu, N, and O atoms remains in good agreement with that deduced from EPR. The magnitudes of the  $^{14}\text{N}$  hyperfine constants along with copper  $T_{zz}$  and  $a_{\text{iso}}$  are reproduced fairly well; however, for the  $T_{yy}$  and  $T_{xx}$  components of the dipolar  $^{63}\text{Cu}$  superhyperfine tensor, the agreement with experiment is less satisfactory because of an artificial polarization of the  $3d_{yz}$  orbital. The distribution of the spin density around the copper nucleus is very sensitive to the calculation method, and it is shifted from Cu to the NO ligand with an admixture of exact exchange.

**Acknowledgment.** The calculations were performed using computer facilities of the Academic Computer Center CYFRO-NET-CRACOW and were sponsored by Komitet Badań Naukowych (grant number KBN/SGI2800/UJ/018/2002). Z.S. thanks the Pruszyński Foundation for the A. Krzyżanowski stipend.

#### References and Notes

- Iwamoto, M.; Hamada, H. *Catal. Today* **1991**, *10*, 57.
- Sojka, Z.; Che, M.; Giamello, E. *J. Phys. Chem. B* **1997**, *101*, 4831.
- Spoto, G.; Bordiga, S.; Scarano, D.; Zecchina, A. *Catal. Lett.* **1992**, *13*, 39.
- Poepl, A.; Hartmann, M. *Stud. Surf. Sci. Catal.* **2002**, *142*, 375.
- DeGray, J. A.; Rieger, P. H. *Bull. Magn. Reson.* **1987**, *8*, 95.
- Eriksson, L. A.; Malkina, O. L.; Malkin, V. G.; Salahub, D. R. *J. Chem. Phys.* **1994**, *100*, 5066.
- Wetmore, S. D.; Boyd, R. J.; Eriksson, L. A. *J. Chem. Phys.* **1997**, *106*, 7738.
- Gauld, J. W.; Eriksson, L. A.; Radom, L. *J. Phys. Chem. A* **1997**, *101*, 1352.
- Jaszewski, A. R.; Jezierska, J.; Jezierski A. *Chem. Phys. Lett.* **2000**, *319*, 611.
- Barone, V. *Chem. Phys. Lett.* **1996**, *262*, 201.
- Giamello, E.; Paganini, M. C.; Murphy, D. M.; Ferrari, A. M.; Pacchioni G. *J. Phys. Chem. B* **1997**, *101*, 971.
- Chiesa, M.; Giamello, E.; Murphy, D. M.; Pacchioni, G.; Paganini, M. C.; Soave, R.; Sojka, Z. *J. Phys. Chem. B* **2001**, *105*, 497.
- Munzarova, M.; Kaupp, M. *J. Phys. Chem. A* **1999**, *103*, 9966.
- Barden, D. A.; Tyler, D. R. *J. Am. Chem. Soc.* **1998**, *120*, 942.
- Munzarova, M.; Kubacek, P.; Kaupp, M. *J. Am. Chem. Soc.* **2000**, *122*, 11900.
- Larsen, S. C. *J. Phys. Chem. A* **2001**, *105*, 8333.
- Swann, J.; Westmoreland, T. D. *Inorg. Chem.* **1997**, *36*, 5348.
- Stadler, C.; de Lacey, A.; Hernandez, B.; Fernandez, V. M.; Conesa, J. C. *Inorg. Chem.* **2002**, *41*, 4417.
- Patchkovskii, S.; Ziegler, T. *J. Am. Chem. Soc.* **2000**, *122*, 3506.
- Pierloot, K.; Delabie, A.; Groothaert, M. H.; Schooheydt, R. A. *Phys. Chem. Chem. Phys.* **2001**, *3*, 2174.
- Carl, P. J.; Isley, S. L.; Larsen, S. C. *J. Phys. Chem. A*, **2001**, *105*, 4563.
- Ruggiero, C. E.; Carrier, S. M.; Antholine, W. E.; Whittaker, J. W.; Cramer, C. J.; Tolman, W. B. *J. Am. Chem. Soc.* **1993**, *115*, 11285.
- Weil, J. A.; Bolton, J. R.; Wertz, J. E. *Electron Paramagnetic Resonance: Elementary Theory and Practical Applications*; Wiley & Sons: New York, 1994.
- Malkin, V. G.; Malkina, O. L.; Eriksson, L. A.; Salahub, D. R. In *Modern Density Functional Theory: A Tool for Chemistry*; Politzer, P., Seminario, J. M., Eds.; Theoretical and Computational Chemistry; Elsevier: Amsterdam, 1995; Vol. 2.
- Barone, V. *Theor. Chim. Acta* **1995**, *91*, 113.
- Kong, J.; Eriksson, L. A.; Boyd, R. J. *Chem. Phys. Lett.* **1994**, *217*, 24.
- Broclawik, E.; Datka, J.; Gil, B.; Kozyra, P. *Phys. Chem. Chem. Phys.* **2000**, *2*, 401.
- DMol, InsightII release 95.0; Biosym/MSI: San Diego, CA, 1995.
- Vosko, S. H.; Wilk, L.; Nusair, M. *Can. J. Phys.* **1980**, *58*, 1200.
- Becke, A. D. *Phys. Rev. A* **1988**, *38*, 3098.
- Perdew, J. P.; Wang, Y. *Phys. Rev. B* **1992**, *45*, 13244.
- Hirshfeld, F. L. *Theor. Chim. Acta* **1977**, *44*, 129.
- Treesukol, P.; Limtrakul, J.; Truong, T. N. *J. Phys. Chem. B* **2001**, *105*, 2421.
- Frisch, M. J.; Trucks, G. W.; Schlegel, H. B.; Scuseria, G. E.; Robb, M. A.; Cheeseman, J. R.; Zakrzewski, V. G.; Montgomery, J. A., Jr.; Stratmann, R. E.; Burant, J. C.; Dapprich, S.; Millam, J. M.; Daniels, A. D.; Kudin, K. N.; Strain, M. C.; Farkas, O.; Tomasi, J.; Barone, V.; Cossi, M.; Cammi, R.; Mennucci, B.; Pomelli, C.; Adamo, C.; Clifford, S.; Ochterski, J.; Petersson, G. A.; Ayala, P. Y.; Cui, Q.; Morokuma, K.; Malick, D. K.; Rabuck, A. D.; Raghavachari, K.; Foresman, J. B.; Cioslowski, J.; Ortiz, J. V.; Stefanov, B. B.; Liu, G.; Liashenko, A.; Piskorz, P.; Komaromi, I.; Gomperts, R.; Martin, R. L.; Fox, D. J.; Keith, T.; Al-Laham, M. A.; Peng, C. Y.; Nanayakkara, A.; Gonzalez, C.; Challacombe, M.; Gill, P. M. W.; Johnson, B. G.; Chen, W.; Wong, M. W.; Andres, J. L.; Head-Gordon, M.; Replogle, E. S.; Pople, J. A. *Gaussian 98*, revision A.11.4; Gaussian, Inc.: Pittsburgh, PA, 1998.
- Rieger, P. H. *J. Magn. Reson.* **1997**, *124*, 140.
- Bowker, H. J.; Symons, M. C. R.; Tinling, D. J. A. In *Radical Ions*; Kaiser, E. T., Kevan, L., Eds.; Interscience: New York, 1968.
- van Koningsveld, H.; Jansen, J. C.; van Bekkum, H. *Zeolites* **1990**, *10*, 235.
- Sayle, D. C.; Richard, C.; Catlow, A.; Gale, J. D.; Perrin, M. A. *J. Phys. Chem.* **1997**, *101*, 3331.
- Nachtigalova, D.; Nachtigal, P.; Sierka, M.; Sauer, J. *Phys. Chem. Chem. Phys.* **1999**, *1*, 2019.
- Lamberti, C.; Bordiga, S.; Salvalaggio, M.; Spoto, G.; Zecchina, A.; Geobaldo, F.; Vlaic, G.; Bellatreccia, M. *J. Phys. Chem. B* **1997**, *101*, 344.
- Dedeczek, J.; Sobalik, Z.; Tvaruzkova, Z.; Kaucky, D.; Wichterlova, B. *J. Phys. Chem.* **1995**, *99*, 16327.
- Nachtigalova, D.; Nachtigal, M.; Sauer, J. *Phys. Chem. Chem. Phys.* **2001**, *3*, 1552.
- Sierraalta, A.; Anez, R.; Brussa, M. R. *J. Catal.* **2002**, *205*, 107.
- Santiago, L. R.; Sierka, M.; Branchadell, V.; Sodupe, M.; Sauer, J. *J. Am. Chem. Soc.* **1998**, *120*, 1545.
- Sayle, D. C.; Richard, C.; Catlow, A.; Gale, J. D.; Perrin, M. A.; Nortier, P. *J. Phys. Chem. A* **1997**, *101*, 3331.
- Broclawik, E.; Datka, J.; Gil, B.; Kozyra, P. *Int. J. Mol. Sci.* **2002**, *3*, 435.
- Troub, B. L.; Chakraborty, A. K.; Bell, A. T. *J. Phys. Chem.* **1996**, *100*, 4173.
- Koch, W.; Holthausen, M. C. A *Chemist's Guide to Density Functional Theory*; Wiley-VCH: Weinheim, Germany, 2000; p 127.
- Scheidt, W. R.; Ellison, M. K. *Acc. Chem. Res.* **1999**, *32*, 350.
- Bauschlicher, C. W., Jr.; Langhoff, S. R.; Partridge, H. *J. Chem. Phys.* **1991**, *94*, 2068.
- Hay, P. J.; Wadt, W. R. *J. Chem. Phys.* **1985**, *82*, 270.
- Pople, J. A.; Gill, P. M. W.; Handy, N. C. *Int. J. Quantum Chem.* **1995**, *56*, 303.
- Mabbs, F. E.; Collison, D. *Electron Paramagnetic Resonance of d Transition Metal Compounds*; Elsevier: Amsterdam, 1992.
- Bernardi, F.; Bottoni, A.; Calcinari, M.; Rossi, I. *J. Phys. Chem. A* **1997**, *101*, 6310.
- Broclawik, E.; Borowski, T. *Chem. Phys. Lett.* **2001**, *339*, 433.
- Peake, B. M.; Rieger, P. H.; Robinson, B. H.; Simpson, J. *J. Am. Chem. Soc.* **1980**, *102*, 156.